Inorganic Chemistry

Article

pubs.acs.org/IC

Manganese–Vanadate Hybrids: Impact of Organic Ligands on Their Structures, Thermal Stabilities, Optical Properties, and Photocatalytic Activities

Lan Luo,[†] Yuhan Zeng,[†] Le Li,[†] Zhixiang Luo,[‡] Tatyana I. Smirnova,[†] and Paul A. Maggard*[,†]

[†]Department of Chemistry, North Carolina State University, Raleigh, North Carolina 27695-8204, United States

[‡]Department of Physics and Astronomy, University of North Carolina at Chapel Hill, North Carolina 27599-3255, United States

Supporting Information

ABSTRACT: Manganese(II)–vanadate(V)/organic hybrids were prepared in high purity using four different N-donor organic ligands (2,6:2′,2″-terpyridine = terpy, 2,2′-bipyrimidine = bpym, *o*-phenanthroline = *o*-phen, and 4,4′-bipyridine = 4,4′-bpy), and their crystalline structures, thermal stabilities, optical properties, photocatalytic activities and electronic structures were investigated as a function of the organic ligand. Hydrothermal reactions were employed that targeted a 1:2 molar ratio of Mn(II)/V(V), yielding four hybrid solids with the compositions of $Mn(terpy)V_2O_6{\cdot}H_2O$ (**I**), $Mn_2(bpym)V_4O_{12}{\cdot}0.6H_2O$ (**II**), $Mn(H_2O)(o\text{-phen})V_2O_6$ (**III**), and $Mn(4,4'\text{-bpy})V_2O_6{\cdot}1.16H_2O$ (**IV**). The inorganic component within these hybrid compounds, that is, $[MnV_2O_6]$, forms infinite chains in **I** and layers in **II**, **III**, and **IV**. In each case, the organic ligand preferentially coordinates to the Mn(II) cations within their respective structures, either as chelating and three-coordinate (mer isomer in **I**) or two-coordinate (cis isomers in **II** and **III**), or as bridging and two coordinate (trans isomer in **IV**). The terminating ligands in **I** (terpy) and **III** (*o*-phen) yield nonbridged "MnV_2O_6" chains and layers, respectively, while the bridging ligands in **II** (bpym) and **IV** (4,4′-bpy) result in three-dimensional, pillared hybrid networks. The coordination number of the ligand, that is, two- or three-coordinate, has the predominant effect on the dimensionality of the inorganic component, while the connectivity of the combined metal-oxide/organic network is determined by the chelating versus bridging ligand coordination modes. Each hybrid compound decomposes into crystalline MnV_2O_6 upon heating in air with specific surface areas from ∼7 m^2/g for **III** to ∼41 m^2/g for **IV**, depending on the extent of structural collapse as the lattice water is removed. All hybrid compounds exhibit visible-light bandgap sizes from ∼1.7 to ∼2.0 eV, decreasing with the increased dimensionality of the $[MnV_2O_6]$ network in the order of **I** > **II** ≈ **III** > **IV**. These bandgap sizes are smaller by ∼0.1–0.4 eV in comparison to related vanadate hybrids, owing to the addition of the higher-energy 3d orbital contributions from the Mn(II) cations. Each compound also exhibits temperature-dependent photocatalytic activities for hydrogen production under visible-light irradiation in 20% methanol solutions, with threshold temperatures of ∼30 °C for **III**, ∼36 °C for **I**, and ∼40 °C for **II**, **IV**, and $V_4O_{10}(o\text{-phen})_2$. Hydrogen production rates are ∼142 μmol H_2 $g^{-1}{\cdot}h^{-1}$, ∼673 μmol H_2 $g^{-1}{\cdot}h^{-1}$, ∼91 μmol H_2 $g^{-1}{\cdot}h^{-1}$, and ∼218 μmol H_2 $g^{-1}{\cdot}h^{-1}$ at 40 °C, for **I**, **II**, **III**, and **IV**, respectively, increasing with the oxide/organic network connectivity. In contrast, the related $V_4O_{10}(o\text{-phen})_2$ exhibits a much lower photocatalytic rate of ∼36 H_2 $g^{-1}{\cdot}h^{-1}$. Electronic structure calculations based on density-functional theory methods show that the valence band edges are primarily derived from the half-filled Mn $3d^5$ orbitals in each, while the conduction band edges are primarily comprised of contributions from the empty V $3d^0$ orbitals in **I** and **II** and from ligand π^* orbitals in **III**. Thus, the coordinating organic ligands are shown to significantly affect the local and extended structural features, which has elucidated the underlying relationships to their photocatalytic activities, visible-light bandgap sizes, electronic structures, and thermal stabilities.

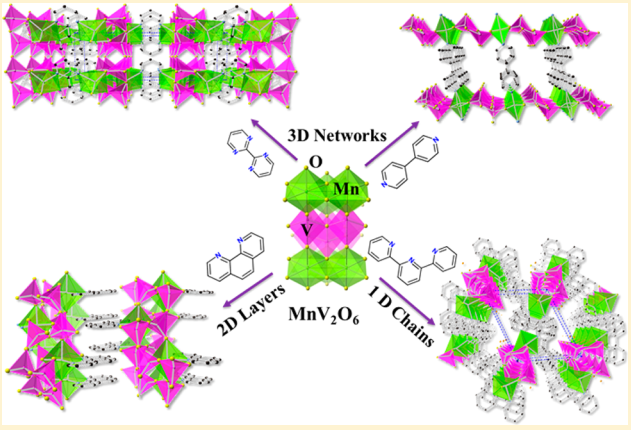

I. INTRODUCTION

Metal oxide/organic hybrid compounds represent a large and rapidly growing class of materials that combine the molecular-level tunability of coordinating organic ligands with the robust physical properties of metal oxides. This class of compounds yields a diversity of crystalline frameworks with potential uses in biomedicine,[1] gas storage,[2] energy storage,[3] photocatalysis, and many other applications.[4,5] Within the broader family of inorganic/organic hybrids, which includes the expansive family

Received: April 24, 2015
Published: July 23, 2015

DOI: 10.1021/acs.inorgchem.5b00931
Inorg. Chem. 2015, 54, 7388–7401

of purely metal−organic networks, the metal oxide/organic hybrid compounds distinguish themselves by their extended $[-O-M-O-M-O-]_n$ connectivity.[6−8] The incorporated organic ligands function in various ways that impact their overall crystalline structures, such as by (a) charge-balancing packing effects, (b) alteration of the local coordination environments of different metal centers, and (c) the overall framework dimensionality, for example, of bridging versus chelating ligands. This class of hybrids provides a rich structural diversity and a growing ability both to maintain an extended metal oxide connectivity and to tune its physical properties as a function of the flexible crystalline frameworks.

Vanadate/organic hybrid compounds have been of particular interest owing to the optical and photocatalytic properties of the related condensed vanadates, for example, $BiVO_4$, Ag_3VO_4, and $InVO_4$, which are reportedly active for dye degradation and water splitting when irradiated at visible-light wavelengths.[9−11] The vanadate hybrid compounds have yielded a number of closely related structures containing extended homometallic $[-O-V-O-V-O-]_n$ and heterometallic $[-O-V-O-M-O-]_n$ (M = Ag, Cu, Mn) connectivity, as reviewed previously.[12a,12b] Recently reported examples include $Ag_4(pzc)_2V_2O_6$ (pzc = pyrazine-2-carboxylate),[13] Co(bimb)-V_2O_6 (bimb = 1,3-bis(1-imidazolyl)benzene),[14] and Mn(2,2′-bpy)V_4O_{10}(2,2′-bpy),[15] as well as others.[16,17] In each of these cases the fundamental bandgap transition originates from a metal-to-metal charge transfer transition, that is, between the filled Ag $4d^{10}$ and empty V $3d^0$ orbitals in $Ag_4(pzc)_2V_2O_6$. Importantly, their bandgap sizes fall within the visible-light wavelengths, thus facilitating their potential use with the solar spectrum to drive photocatalytic reactions for either water purification or hydrogen production.[13,15] The relatively few examples reported so far have already enabled a beginning understanding of the structural and electronic origins of their photocatalytic activities when irradiated in aqueous solutions. However, relatively few prior investigations have focused on the systematic preparation of a family of related hybrid compounds that enables a deeper investigation of the key relationships between their photocatalytic properties, bandgap sizes, and crystalline structures.

The incorporation of high-spin Mn(II) cations into the structures of vanadates has been shown to result in a significant red-shifting of their bandgap sizes, for example, up to ∼0.6 eV more deeply into the visible-light wavelengths.[18] In manganese−vanadate hybrids, the recently reported Mn(2,2′-bpy)-V_4O_{10}(2,2′-bpy) and $(NH_4)_2[\{Mn(salen)(H_2O)\}_6V_6O_{18}]$-$(NO_3)_2$·$30H_2O$ have been found to exhibit photocatalytic activity for dye decomposition or the production of oxygen and hydrogen from aqueous solutions under ultraviolet and visible-light irradiation.[15,17] Additional investigations are thus critical to better understand the impact of the organic ligands and the resulting structural connectivities of the two transition-metal cations in this system, that is, comprised of Mn(II) and V(V) cations, on their physical and chemical properties. Herein is described the syntheses, crystalline structures, optical bandgap sizes, and photocatalytic activities of a family of related Mn(II)−vanadate hybrids prepared using four ligands with varying lengths and geometric arrangements of N-donor atoms, as shown in Scheme 1. Described below, investigations within this family include the hydrothermal synthesis of the two new compounds Mn(terpy)V_2O_6·H_2O (**I**) and Mn_2(bpym)V_4O_{12}·$0.6H_2O$ (**II**), as well as new synthetic procedures to prepare the two related Mn(H_2O)(*o*-phen)V_2O_6 (**III**) and Mn(4,4′-bpy)-V_2O_6·$1.16H_2O$ (**IV**) in high purity for physical property measurements. Analysis of their crystalline structures with respect to the effects of the ligand geometries and coordination modes is used to investigate relationships to their optical bandgap sizes, photocatalytic activities, and thermal stabilities. Electronic-structure calculations were also employed to probe the structural origins of their conduction and valence band edges.

Scheme 1. Four Selected N-Donor Coordinating Ligands and Illustrations of Their Different Preferred Coordination Modes[a]

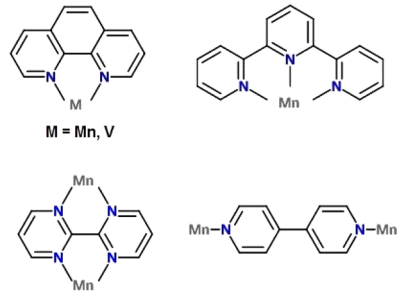

[a]From upper left: *o*-phenanthroline, terpyridine, 4,4′-bpy, and bipyrimidine.

II. EXPERIMENTAL SECTION

A. Materials. All reagents were used as supplied by the manufacturer without further purification, including $Mn(OAc)_2$·$4H_2O$ (98%, Alfa Aesar), NH_4VO_3 (99.99%, Aldrich), 2,6:2′,2″-terpyridine (terpy, 97%, Alfa Aesar), 2,2′-bipyrimidine (bpym, 98+%, Alfa Aesar), *o*-phenanthroline (*o*-phen, 99+%, Aldrich), 4,4′-bipyridine (4,4′-bpy, 99%, Alfa Aesar), and glacial acetic acid (99.7%, Fisher Chemical). A reagent amount of deionized water was also used in each hydrothermal reaction.

B. Synthetic Procedures. Hybrid compounds **I** to **IV** were prepared using hydrothermal synthetic techniques by loading stoichiometric amounts of reactants and deionized water into polytetrafluoroethylene Teflon pouches (3″ × 3″) that were then heat-sealed in air. These pouches were placed into 125 mL polytetrafluoroethylene-lined stainless-steel autoclaves that were backfilled with ∼40 mL of deionized water before closing. The reaction vessel was heated in a convection oven with the following temperature programs: For **I**: 140 °C for 10 h, then ramping to 180 °C in 5 h, then 180 °C for 15 h; **II**: 150 °C for 10 h; **III**: 180 °C for 48 h; and **IV**: 180 °C for 15 h. All reactions were subsequently slowly cooled to room temperature at a rate of 6 °C/h. The products were washed with deionized water, collected, and dried at 60 °C overnight. Each hybrid compound could be obtained in high phase purity (>95%) according to powder X-ray diffraction (XRD) data (Figure S1 in Supporting Information). All percent yields were calculated based on the amount of vanadium.

Mn(terpy)V_2O_6·H_2O (**I**) was synthesized by a reaction of 0.0060 g of $Mn(OAc)_2$·$4H_2O$, 0.0029 g of NH_4VO_3, 0.0049 g of terpyridine, 0.0126 g of glacial acetic acid, and 2 mL of H_2O that gave a molar ratio of 1:1:0.85:8:4500. Large brown-colored cubic crystals of **I** were obtained in a yield of ∼70%.

Mn_2(bpym)V_4O_{12}·$0.6H_2O$ (**II**) was prepared by mixing 0.0173 g of $Mn(OAc)_2$·$4H_2O$, 0.0331 g of NH_4VO_3, 0.0392 g of bipymidine, 0.0213 g of glacial acetic acid, and 2 mL of H_2O in a molar ratio of 2:8:7:10:3000. A small amount of orange-colored fine powder can be removed by dispersing the resulting brown crystals in ∼30 mL of water and sonicating for 20−30 s. The water (containing the orange-colored powder) was poured off after allowing the brown-colored crystals to settle for ∼1−2 min. This sonication/separation process was repeated three times until a high purity was achieved, as judged by powder XRD

DOI: 10.1021/acs.inorgchem.5b00931
Inorg. Chem. 2015, 54, 7388−7401

and visually under a microscope. Large, dark, brown-colored, block crystals of **II** were obtained in a yield of ∼37%.

The synthesis of $Mn(H_2O)(o\text{-phen})V_2O_6$ (**III**) has been reported previously.[19] An intermediate-based two-step preparation resulting in a higher purity was found utilizing $V_4O_{10}(o\text{-phen})_2$ and $Mn(o\text{-phen})_2Cl_2$ as intermediates. In this reaction pathway, $V_4O_{10}(o\text{-phen})_2$ is first prepared by reacting 0.0496 g of NH_4VO_3, 0.0420 g of *o*-phenanthroline, 0.0281 g of glacial acetic acid, and ∼2 mL of H_2O in a molar ratio of 1:1.1:2.2:∼1000 at 140 °C for 10 h. This synthesis of $V_4O_{10}(o\text{-phen})_2$ is similar to previously reported procedures,[20] but the product is obtained in a relatively higher yield of ∼79%. The $Mn(o\text{-phen})_2Cl_2$ precursor was also prepared according to a previously reported procedure.[21] In the final reaction step, 0.0535 g of $V_4O_{10}(o\text{-phen})_2$ is reacted under hydrothermal conditions with 0.2873 g of $Mn(o\text{-phen})_2Cl_2$, within a solvent consisting of 0.177 g of glacial acetic acid and ∼2 mL of H_2O. Large brown-colored cubic crystals and a fine powder of **III** were obtained in a yield of ∼75%, as well as some unreacted $Mn(o\text{-phen})_2Cl_2$ (yellow crystals). The excess reactant can be separated by grinding the mixture into fine powder, such that $Mn(o\text{-phen})_2Cl_2$ becomes soluble in water.

The synthesis of $Mn(4,4'\text{-bpy})V_2O_6{\cdot}1.16H_2O$ (**IV**) has been reported previously.[22] A somewhat shorter synthesis time and a higher yield can be obtained by a hydrothermal reaction of 0.0089 g of $Mn(OAc)_2{\cdot}4H_2O$, 0.0127 g of NH_4VO_3, 0.0170 g of 4,4-bipydine, 0.0219 g of glacial acetic acid, and ∼2 mL of H_2O in a molar ratio of 1:3:3:10:∼3000. Light brown-colored, aggregated, crystallites were obtained on the surface of the reaction pouches in a yield of ∼45%, with a small amount of darker brown-colored impurities that were manually separated from the product.

C. Structural Characterization. Single-crystal data sets for **I** and **II** were collected on a Bruker APEX-II CCD diffractometer using graphite-monochromatized Mo Kα radiation (λ = 0.710 73 Å) in a sealed tube at 110 K. The initial unit cell determination and data reduction were performed with the use of the Bruker SAINT program.[23] These structures were solved by direct methods, and the structural refinements were performed by full matrix least-squares methods within the software program SHELXS-97.[24] Hydrogen atoms were placed in idealized positions and were fixed to ride on the parent carbon or oxygen atoms of the ligands. Selected crystallographic data and structure refinement parameters for each are given in Table 1. Selected interatomic distances, bond angles, and the results of bond valence sum calculations are listed in Tables 2 and 3.

Table 1. Selected Crystal Data and Refinement Details for I and II

compound	I	II
chemical composition	$C_{15}H_{13}MnN_3O_7V_2$	$C_8H_7Mn_2N_4O_{13}V_4$
crystal system	triclinic	monoclinic
space group, *Z*	$P\bar{1}$, 2	*C*2/*m*, 2
temperature, K	110(2)	110(2)
a, Å	6.907(1)	8.3490(4)
b, Å	11.211(2)	18.953(1)
c, Å	13.094(3)	5.9129(3)
α, deg	106.75(1)	90.00
β, deg	102.05(1)	95.581(3)
γ, deg	106.45(1)	90.00
V, Å^3	883.5(3)	931.20(8)
ρ, g/cm^3	1.895	2.428
μ, mm^{-1}	1.785	3.316
total reflections, R_{int}	9425, 0.0294	6176, 0.0458
data/restraints/parameters	3072/80/256	1117/1/81
final R_1, wR_2[a] [$I > 2\sigma(I)$]	0.0385, 0.1022	0.0347, 0.0818
$\Delta\rho_{max}/\Delta\rho_{min}$, e/Å^3	1.026/−0.447	0.785/−0.950

[a] $R_1 = \sum(|F_o - F_c|)/\sum F_o$; $wR_2 = [\sum(w(F_o^2 - F_c^2)^2)/(\sum(F_o^2)^2)]^{1/2}$; w = σ_F^{-2}.

Table 2. Selected Bond Distances (Å), Angles (deg), and Bond Valence Sums for I[a]

atom1	atom2	distance	intra-polyhedral angles	
Mn	O1	2.145(2)	O1−Mn−O3	90.27(9)
	O2	2.171(2)	O1−Mn−O2	172.7(1)
	O3	2.062(2)	O3−Mn−O2	90.6(1)
	N1	2.185(3)	N1−Mn−O3	170.1(1)
	N2	2.238(3)	N2−Mn−O3	116.4(1)
	N3	2.258(3)	N3−Mn−N2	145.9(1)
	$\sum S_{ij}$	2.243		
V1	O1	1.658(2)	O1−V1−O2	108.6(1)
	O2	1.638(2)	O2−V1−O4	109.3(1)
	O4	1.784(2)	O4−V1− O1	111.3(1)
	O5	1.792(2)	O5−V1− O1	109.7(1)
	$\sum S_{ij}$	5.124		
V2	O3	1.669(2)	O3−V2−O4	111.9(1)
	O4	1.789(2)	O4−V2 −O5	109.1(1)
	O5	1.816(2)	O5−V2−O6	108.8 (1)
	O6	1.610(2)	O6−V2−O3	108.5(1)
	$\sum S_{ij}$	5.002		

[a] $S_{ij} = \exp[(R_0 - R_{ij})/B]$, B = 0.37, R_0 = 1.790 Å for Mn^{II}−O, R_0 = 1.862 Å for Mn^{II}−N, R_0 = 1.803 Å for V^{V}−O.

Table 3. Selected Bond Distances (Å), Angles (deg), and Bond Valence Sums for II[a]

atom1	atom2	distance	intra-polyhedral angles	
Mn	O1	2.088(2)	O1−Mn−O2	91.2(1)
	O2	2.107(2)	O2−Mn−N	84.9(1)
	N	2.267(3)	O1−Mn−N	166.8(1)
	$\sum S_{ij}$	2.41		
V	O1	1.658(2)	O1−V−O2	109.7(1)
	O2	1.648(2)	O2−V−O3	108.8(1)
	O3	1.801(1)	O3−V−O4	110.99(8)
	O4	1.791(1)	O4−V−O1	111.4(1)
	$\sum S_{ij}$	5.028		

[a] $S_{ij} = \exp[(R_0 - R_{ij})/B]$, B = 0.37, R_0 = 1.790 Å for Mn^{II}−O, R_0 = 1.862 Å for Mn^{II}−N, R_0 = 1.803 Å for V^{V}−O.

The crystalline purities of the products in each case were characterized by high-resolution powder XRD data on a RIGAKU R-Axis Spider powder X-ray diffractometer (graphite monochromatized Cu Kα radiation) at room temperature. Powder XRD patterns were scanned with a step size of 0.02° over the 2θ angular range from 4° to 100° and dwell times of 4 s for each step. Mid-infrared (400−4000 cm^{-1}) spectra were measured on an IR-Prestige 21 Shimadzu Fourier transform infrared spectrophotometer (FTIR) equipped with a GladiATR accessory. Approximately 10 mg of high-purity powder was loaded onto the sample stage in each case, and the data were plotted as transmittance versus wavenumber, as shown in Figure S3 in the Supporting Information.

D. Spectroscopic and Thermal Characterization. UV−vis diffuse reflectance spectra (DRS) were measured on a Shimadzu UV-3600/3100 UV−vis−near-IR spectrophotometer equipped with an integrating sphere. A pressed barium sulfate powder tablet was used as the reference. The data were plotted as the remission function $F(R_\infty) = (1 - R_\infty)^2/(2R_\infty)$ versus energy, where R_∞ is diffuse reflectance according to the Kubelka−Monk theory of diffuse reflectance.[25] The optical bandgap sizes were estimated with the use of the formula E_g (eV) = 1240/λ_g(nm), where λ_g is extrapolated from the linear rising part in the spectra.[26] These data are listed in Table 4.

Continuous wave (CW) X-band electron paramagnetic resonance (EPR) spectra were collected using a Varian Century Series EPR spectrometer (Palo Alto, CA) at microwave frequencies of ∼9.5 GHz (X-band). Each solid sample was weighed to the same mass (0.45 mg),

DOI: 10.1021/acs.inorgchem.5b00931
Inorg. Chem. 2015, 54, 7388−7401

Table 4. Bandgap Sizes and Specific Surface Areas for Compounds I to IV, Both before and after Heating in Air and Removing the Coordinating Organic Ligands

	$V_4O_{10}(o\text{-phen})_2$	I	II	III	IV
direct transition (eV)	2.40	2.24	2.65	2.56	2.17
indirect transition (eV)	2.10	1.95	1.83	1.89	1.68
specific surface area (m^2/g)	3.6	8.7	6.6	2.3	8.8
indirect transition after removal of ligands in air (eV)[a]	2.23	1.69	1.64	1.72	1.77
specific surface areas after the removal of ligands in air (m^2/g)	3.5	15	16	7.1	41

[a]According to powder XRD, the products after ligand removal corresponded to V_2O_5 for $V_4O_{10}(o\text{-phen})_2$ and to MnV_2O_6 for each of the hybrids **I** to **IV**.

settled to the bottom of a 3 mm quartz EPR tube, and then placed into a resonator. CW EPR spectra were digitized to 2048 data points per spectrum. Typical spectrometer settings were as follows: microwave power of 2 mW (20 dB attenuation), field modulation frequency of 100 kHz, and field modulation amplitude of 10 G. The temperature-controlled measurements were performed using a variable-temperature accessory as previously described.[27]

Scanning electron microscopy (SEM) images of the products were taken on a Hitachi S-4700 cold cathode field-emission scanning electron microscope operating at 2.0–20 kV, depending on the conductivity of the material. All samples were coated with an ~3 nm Au/Pd layer by a Cressington 108 auto sputter coater prior to the measurement to prevent charging accumulation in the SEM. Energy dispersive spectroscopy (Oxford Instrument, INCA PentaFET-x3) was utilized to confirm the chemical compositions and surface platinum deposition (i.e., for the phocotatalysis measurements) on the metalized samples for photocatalysis.

Thermogravimetric analyses (TGA) were taken on a TA Instruments TGA Q50 by loading ~0.0050 g of sample onto a platinum pan. The pan was equilibrated and tared at room temperature and heated to 600 °C at a rate of 10 °C/min under flowing N_2 and air. The post-heated TGA residues were characterized by powder XRD, as described above. Specific surface areas of the hybrid compounds and their post-heated TGA residues were measured on a Quantachrome ChemBET Pulsar TPR/TPD. Samples were preheated to 140 °C under flowing N_2 to degas for 3 h and then cooled with liquid nitrogen and analyzed using a 30% He/N_2 gas mixture.

E. Measurements of Photocatalytic Activities. Photocatalytic activities for hydrogen production were measured by suspending a weighed amount (~10 mg) of each powdered sample coated with 1% platinum in an outer-irradiation range quartz reaction cell that was filled with 45 mL of a 20% aqueous methanol solution. To remove any trapped gases on the particle surfaces, the particle suspension was first stirred in the dark for ~0.5 h with constant nitrogen bubbling and then sonicated in degas mode for 90 min. This sonication step is necessary to observe the subsequent photocatalytic activity. The reaction cell was then irradiated under an 800 W high-pressure Xe arc lamp (Newport Oriel 6271, focused through a shutter window), which was equipped with an external fan, an IR water filter, and visible-light cutoff filters (λ > 420 nm). The reaction temperature was controlled by an external heater and monitored every 15 min. The temperature was slowly increased until a measurable amount of hydrogen was produced after an initial reaction time of 15 min. Measurable rates for photocatalytic activities were found at 30 °C for **III**, at 36 °C for **I**, and at 40 °C for **II**, **IV**, and $V_4O_{10}(o\text{-phen})_2$. The solution was irradiated with continuous stirring under visible light at an irradiant power density of ~1 W/cm^2. The reaction cell was connected to an L-shaped horizontal quartz tube to collect the evolved gas. The amount of the gases produced was determined volumetrically every 30 min. The collected gas was manually injected into a gas chromatograph (SRI MG No. 2; thermal conductivity detector) to identify the generated gases and to confirm a constant molar ratio over time. Only hydrogen gas was detected by gas chromatography. Carbon dioxide was not detected in the gaseous products, as might usually arise when methanol is used as the sacrificial hole scavenger (i.e., $CH_3OH + H_2O \rightarrow 3H_2 + CO_2$). Tollen's tests and measured pH changes were used to confirm formic acid as the primary oxidation product for photocatalytic reactions involving **II** and **IV** (i.e., $CH_3OH + H_2O \rightarrow 2H_2 + HCOOH$), while formaldehyde is found from photocatalytic reactions using **I** and **III** (i.e., $CH_3OH \rightarrow H_2 + HCOH$). These results are further discussed below.

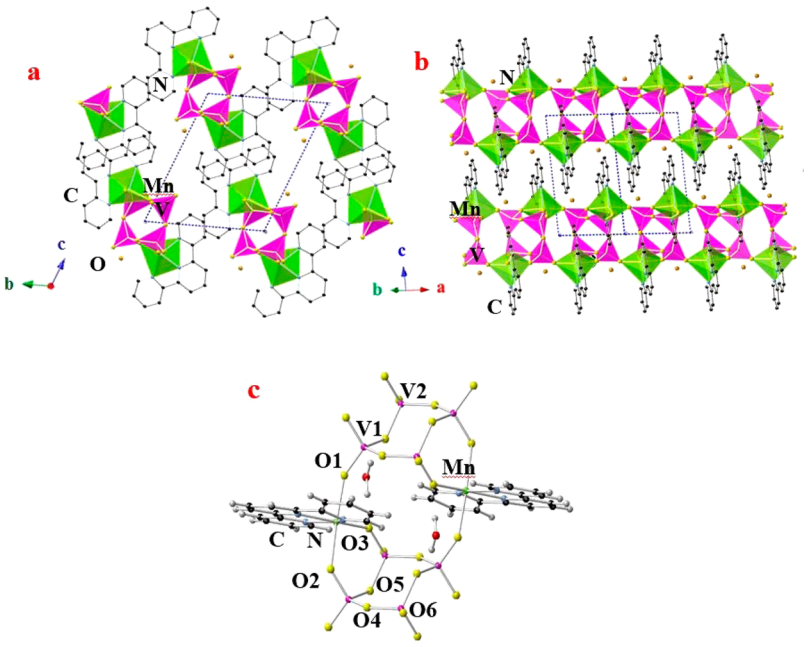

Figure 1. (a, b) Extended structural views of $Mn(terpy)V_2O_6{\cdot}H_2O$ (**I**) and (c) a ball-and-stick representation of the local coordination environments with selected atoms labeled.

DOI: 10.1021/acs.inorgchem.5b00931
Inorg. Chem. 2015, 54, 7388–7401

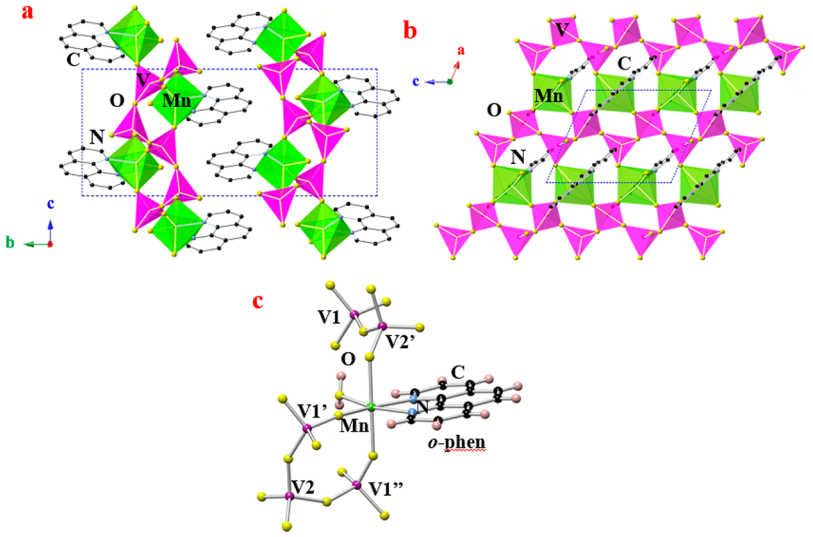

Figure 2. (a, b) Extended structural views of $Mn(H_2O)(o\text{-phen})V_2O_6$ (**III**) and (c) a ball-and-stick representation of the local coordination environments with selected atoms labeled.

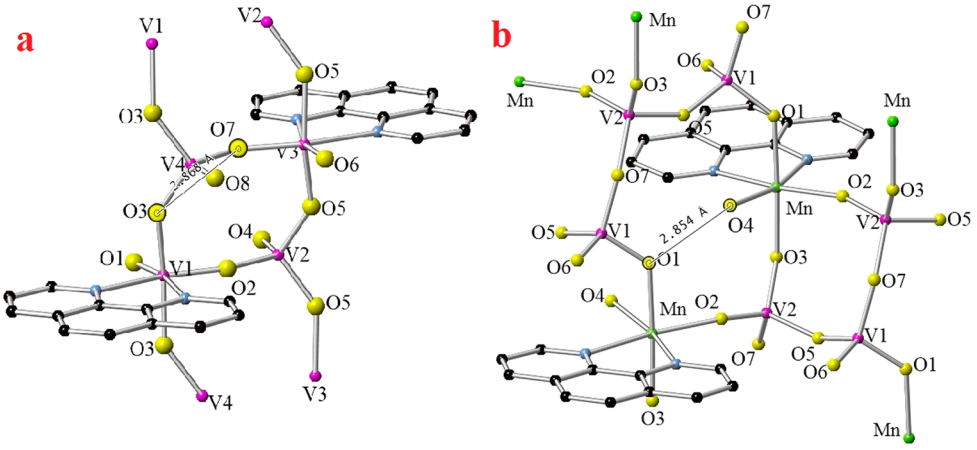

Figure 3. A comparison of the local coordination environments of $V_4O_{10}(o\text{-phen})_2$ (a) and **III** (b), with selected atoms labeled in each.

F. Electronic Structure Calculations. Electronic structure calculations were performed within the CASTEP program package using density functional theory methods.[28] The lattice dimensions and atomic positions were obtained from each of the respective single crystal structures for **I** to **IV**. The Perdew–Burke–Ernzerhof functional in the generalized gradient approximation and ultrasoft Vanderbilt-type pseudopotentials were utilized in the calculations.[29] Equally distributed *k*-points within the Brillouin zone were automatically calculated based on the Monkhorst–Pack scheme.[30]

III. RESULTS AND DISCUSSION

A. Description of Synthetic and Structural Approach. Hydrothermal syntheses of manganese(II)–vanadate/organic hybrid structures were targeted with chemical compositions having a 1:2 Mn-to-V molar ratio, which also incorporated either chelating ligands (i.e., terpy or *o*-phen) or bridging ligands (i.e., bpym or 4,4′-bpy), as shown in Scheme 1. As described below, the synthesized hybrid structures can be classified according to the influence of the ligands on the (i) local Mn(II) coordination environments, (ii) the extended metal-oxide connectivity (i.e., one-dimensional or two-dimensional), and (iii) the combined oxide/organic-network connectivity.

i. Chelating Organic Ligands. a. Mn(terpy)$V_2O_6\cdot H_2O$ (I). The structure of **I**, shown in Figure 1, consists of $[MnV_2O_6]_n$ chains that are oriented down the *a*-axis direction, including two symmetry-inequivalent vanadium atoms and one type of manganese atom. These chains are constructed from cyclic $V_4O_{12}^{4-}$ rings that are each oxo-bridged to four neighboring Mn(II) cations. Each Mn(II) cation is coordinated to one terpyridine ligand (Mn–N at 2.185(3)–2.258(3) Å) and to the bridging oxygen atoms of three different VO_4 tetrahedra (Mn–O at 2.062(2)–2.171(2) Å), forming a distorted Mn(terpy)O_3 octahedral coordination environment shown in Figure 1c. The cyclic $V_4O_{12}^{4-}$ rings are comprised of four VO_4 tetrahedra that are each bridged via two of their vertices with V–O distances of 1.610(2)–1.816(2) Å, consistent with distances reported in prior vanadate structures.[20] A full set of interatomic distances is listed in Table 2. The overall structure can be described as the stacking of these one-dimensional chains with π–π distances between the terpy ligands of ∼3.4 Å, which is close to that typically observed for π–π interactions at ∼3.3 Å to ∼3.5 Å.[31] The infrared spectrum, Figure S3 in the Supporting Information, shows intense sharp peaks in the range from 1600 to 880 cm^{-1} arising from the terpyridine ligand.[32] Relatively broader peaks in the range of 440–900 cm^{-1}

DOI: 10.1021/acs.inorgchem.5b00931
Inorg. Chem. 2015, 54, 7388–7401

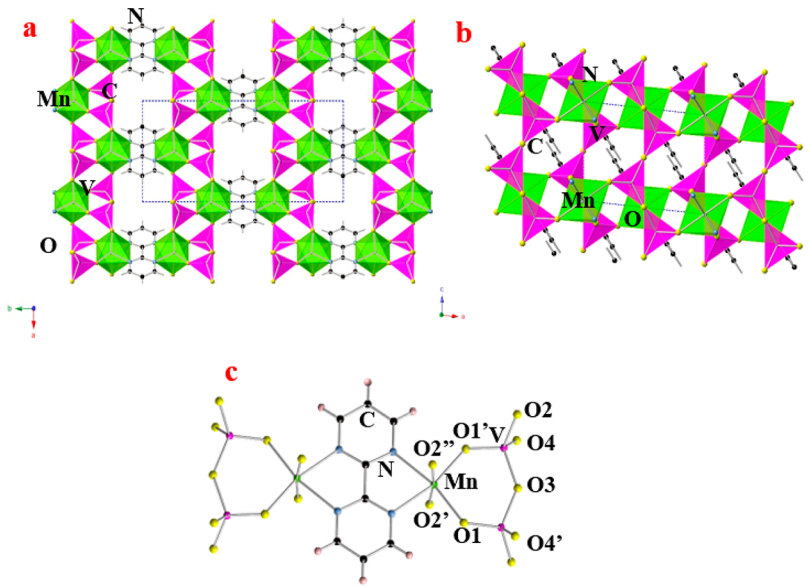

Figure 4. (a, b) Extended structural views of $Mn_2(bpym)V_4O_{12}{\cdot}0.6H_2O$ (**II**) and (c) a ball-and-stick representation of the local coordination environments with selected atoms labeled.

correspond to the Mn−O and V−O vibrations,[33,34] while a broad peak from 3300 to 3600 cm^{-1} is consistent with the lattice water molecule.

b. $Mn(H_2O)(o\text{-phen})V_2O_6$ (III). A novel two-step synthetic route to obtain **III** in high purity was discovered based on the reaction of $V_4O_{10}(o\text{-phen})_2$ with $Mn(o\text{-phen})_2Cl_2$ as intermediates. This synthetic approach was suggested by the structural similarity of $V_4O_{10}(o\text{-phen})_2$ and **III**, which can be viewed as interconvertible through the partial exchange of vanadium for manganese, each of which is coordinated by the *o*-phen ligand in their respective structures (as described below). Shown in Figure 2 is an overall structural view of **III** down the *a*-axis, with the unit cell outlined. As described previously,[19] the structure is comprised of stacked $[MnV_2O_6]$ layers that are coordinated above and below by the *o*-phenanthroline ligand. Within these layers, chains of vertex-bridged VO_4 tetrahedra are linked through $Mn(H_2O)(o\text{-phen})O_3$ octahedra to form the extended layers within the (101) plane. Shown in Figure 2c, each $Mn(H_2O)(o\text{-phen})O_3$ octahedron consists of Mn(II) coordinated to one water molecule, two nitrogen atoms from *o*-phen, and three oxygen atoms from three different VO_4 tetrahedra. Peaks in the infrared spectra in the range from 1600 to 1100 cm^{-1} correspond to the *o*-phen ligand.[21] Similar to **I**, Mn−O and V−O vibrations are found in the range from 400−900 cm^{-1}.

A comparison of the local coordination environments in **III** and in the related $V_4O_{10}(o\text{-phen})_2$ is illustrated in Figure 3. Locally, the structural interconversion between them requires that the two octahedrally-coordinated V atoms in $V_4O_{10}(o\text{-phen})_2$ are replaced by the two Mn(II) cations in **III**. To maintain charge balance within the structure, two additional vanadium and oxygen atoms must be incorporated within **III**, yielding the following (net) substitution pattern: $2\ V^{5+} \rightarrow 2\ Mn^{2+} + 2\ (VO_{2/2})^{3+}$. This results in the Mn atoms in **III** being bridged through two additional VO_4 tetrahedra, as compared to the octahedrally-coordinated vanadium atoms in $V_4O_{10}(o\text{-phen})_2$ that are bridged through two single VO_4 tetrahedra; see Figure 3a,b. The relatively larger Mn(II) versus V(V) cation, that is, ionic radii of 0.80 and 0.47 Å, respectively, as well as the coordinated water molecule, are accommodated by the additional spacing that the two added VO_4 linkages provide. Further, the extra vanadate linkages in **III** lead to its extended layered structure, in comparison to the structure of $V_4O_{10}(o\text{-phen})_2$ that contains only extended vanadate chains. Thus, while the local coordination geometries share many similarities, the extended structural features are significantly altered for charge-balancing and space requirements in the structure of **III**.

c. Structural Impact of Chelating Ligands. The non-bridging chelating ligands, that is, terpyridine and *o*-phen, used in the synthesis of **I** and **III**, result in the inorganic $[MnV_2O_6]$ component forming as either chains or layers, respectively. Each structure contains octahedrally-coordinated manganese and tetrahedrally-coordinated vanadium. However, the terpyridine ligand in **I** coordinates to an additional site on the Mn(II) cation, thus resulting in a lower-dimensional connectivity in the $[MnV_2O_6]_n$ chains versus the $[MnV_2O_6]$ layers in **III**. As each structure contains terminating organic ligands, the overall structural framework is determined by the simple stacking of their respective inorganic chains and layers.

ii. Bridging Organic Ligands. a. $Mn_2(bpym)V_4O_{12}{\cdot}0.6H_2O$ (II). The new structure of **II** is comprised of $[MnV_2O_6]$ layers that are bridged by bpym ligands into a three-dimensional (3D) network, as shown in Figure 4. Selected interatomic distances are listed in Table 3. The $[MnV_2O_6]$ layers are constructed from chains of vertex-bridged VO_4 tetrahedra that run along the *a*-axis and are linked by $Mn(bpym)O_4$ octahedra into layers that are oriented in the (110) plane, shown in Figure 4b. This $[MnV_2O_6]$ layer is structurally similar to that found in the hybrid compound **III**, described above. However, compared to the terminal *o*-phenanthroline ligand in **III**, the bpym ligand in **II** further bridges to a neighboring Mn atom of an adjacent $[MnV_2O_6]$ layer to form an extended 3D network. Thus, the Mn atoms in separate layers are directly adjacent to each other in **II**, owing to the bridging mode of the ligand, but are structurally offset from each other in **III**. A structural view of the local coordination environments is shown in Figure 4c. Each VO_4 tetrahedron is linked through its apical oxygen atoms to two neighboring VO_4 tetrahedra with V−O distances of

DOI: 10.1021/acs.inorgchem.5b00931
Inorg. Chem. 2015, 54, 7388−7401

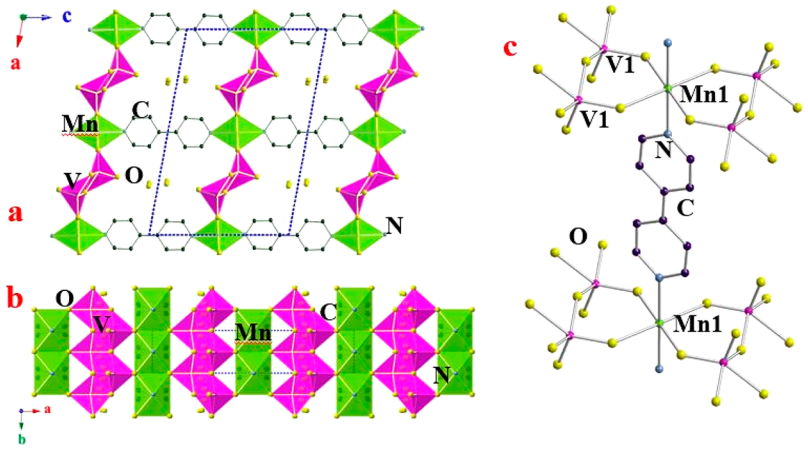

Figure 5. (a, b) Extended views of Mn(4,4′-bpy)V_2O_6·1.16H_2O (**IV**) and (c) a ball-and-stick representation of the local coordination environments with selected atoms labeled.

1.648(2)−1.801(1) Å). The Mn atoms are coordinated to the oxygen atoms of four different VO_4 tetrahedra (Mn−O of 2.088(2) to 2.107(2) Å) and to two nitrogen atoms of a chelating bpym ligand (Mn−N of 2.267(3) Å). The ligand $\pi-\pi$ stacking between adjacent planes occurs at a distance of ∼3.4 Å, similar to that found for **III**. The infrared spectrum shows two sharp peaks centered around 1574 and 1410 cm^{-1} arising from the bpym ligand,[35] and the broad peaks in the range of 470−960 cm^{-1} correspond to Mn−O and V−O vibrations.

b. Mn(4,4′-bpy)V_2O_6·1.16H_2O (IV). Similar to the hybrid structures of **II** and **III**, the structure of **IV** consists of [MnV_2O_6] layers that are bridged together through 4,4′-bpy ligands into a 3D network, as shown in Figure 5a. As described previously,[22] each [MnV_2O_6] layer is constructed from chains of edge-bridged VO_5 square pyramids that run along the *b* axis and are linked by Mn(4,4′-bpy)$_2O_4$ octahedra into layers that are oriented in the (110) plane, shown in Figure 5b. The local coordination environments are shown in Figure 5c. The manganese atoms are coordinated in an octahedral geometry via the nitrogen atoms from two trans-bridging 4,4′-bpy ligands and by the bridging oxygen atoms from four VO_5 square pyramids. These Mn(4,4′-bpy)$_2O_4$ octahedra form an edge-sharing chain along the *b* axis. The structure is similar to that for **II** with the bpym ligand, but with the longer ligand length of 4,4′-bpy in **IV** affording larger interlayer spaces that accommodate additional lattice water molecules that can be easily removed, as described below. The infrared spectrum shows intense absorption peaks centered around 1600−1200 cm^{-1} assigned to the 4,4′-bpy ligand,[36] and peaks in the region of 470−960 cm^{-1} correspond to the Mn−O and V−O vibrations.

c. Structural Impact of Bridging Ligands. The ligands bpym and 4,4′-bpy within the structures of **II** and **IV**, respectively, both yield ligand-bridged [MnV_2O_6] layers. The [MnV_2O_6] layers in **II** are coordinated to bpym and are structurally similar to those in **III** with the *o*-phen ligand, as both ligands coordinate in a cis fashion to the manganese atoms owing to the chelating nature of these ligands. In both **II** and **III**, the four remaining Mn coordination sites have similar geometries in which to coordinate to the vanadate polyhedra within the layers. However, in **IV**, the bridging 4,4′-bpy ligand coordinates to the manganese atoms in a trans fashion, resulting in four remaining Mn coordinate sites in an equatorial geometry and a significantly altered type of [MnV_2O_6] layer. Thus, the cis versus trans coordination geometry of the organic ligand has a significant structural impact on the metal-oxide connectivity within the [MnV_2O_6] layers, while a relatively smaller structural effect is found between similar ligands that are bridging versus nonbridging.

B. Spectroscopic Characterization. Much recent research has shown that hybrid compounds containing a combination of transition metals with empty d^0 (i.e., Nb(V), Mo(VI)) and filled d^{10} or $d^{10}s^2$ (i.e., Ag(I) or Sn(II)) electron configurations can yield decreased visible-light bandgap sizes for use in solar-energy-driven photocatalysis.[9−11] Most recently, progress in this field has expanded to include a new combination of transition metals involving V(V) with Mn(II) cations, including in Mn(2,2′-bpy)V_4O_{10}(2,2′-bpy) and Mn(H_2O)(2,2′-bpy)-V_2O_6 with visible-light bandgap sizes of ∼1.6 and ∼2.2 eV, respectively.[15] Even though both compounds were prepared using 2,2′-bipyridine, the latter compound exhibits a larger bandgap size and no detectable photocatalytic activity, while the former shows a smaller bandgap but significant photocatalytic activity in aqueous solutions for hydrogen and/or oxygen production. Thus, the new series of Mn(II)/V(V) hybrids, that is, **I** to **IV**, were characterized by EPR and UV−vis DRS to better understand the structural, electronic, and optical impacts of the ligand.

The X-band EPR measurements on **I** to **IV** at room temperature, Figures S15 to S18 in the Supporting Information, exhibited signals with varying line widths. Compounds **II** and **III** exhibit single-line spectra with corresponding peak-to-peak widths of 78 and 148 G correspondently with no resolved anisotropy of hyperfine features, while spectra from compounds **I** and **IV** show spectra that are much broader (425 and 312 G) and characteristic of anisotropic g-tensor. The narrower line widths of compounds **II** and **III** are consistent with much shorter Mn−Mn distances (5.4246 Å for compound **II** and 5.5513 Å for compound **III**) compared with compounds **I** and **IV** (6.743 and 7.503 Å, respectively), resulting in collapse of the manganese nuclear hyperfine and g-tensor structure.[37] The effective *g* values for compounds **II** and **III** were calculated to be 1.998(2) and 2.002(2), respectively, and the central and low-field spectral features were observed at 2.010(2) and 2.366(1) for compound **I** and at 2.002(1) and 2.330(1) for compound **IV**, in agreement with the high-spin Mn(II) ions (g = 2.000), in a distorted octahedral coordination environment within each of the structures.[38] The temperature-dependent EPR spectra from

DOI: 10.1021/acs.inorgchem.5b00931
Inorg. Chem. 2015, 54, 7388−7401

300 to 330 K for **I** to **IV** showed a continuous decrease of the EPR signal intensity in each case, consistent with the paramagnetic state of the Mn(II) cation.[22] Bond valence calculations for the manganese sites in each compound are consistent with the Mn(II) and V(V) oxidation states, as listed in Tables 2 and 3 for **I** and **II**.

Optical UV−vis DRS measurements were taken for **I** to **IV**, and the related $V_4O_{10}(o\text{-phen})_2$, to probe the influence of the ligand-based structural modifications, as well as the incorporation of the Mn(II) cation, within their structures. Optical absorptions arising from the (spin-forbidden) d−d transitions on the Mn(II) cations were not observable in any of the spectra. Band gap sizes (indirect) were found in the visible region of energies for each of the Mn(II)/V(V) hybrid compounds, as shown in the Tauc plots in Figure 6. The

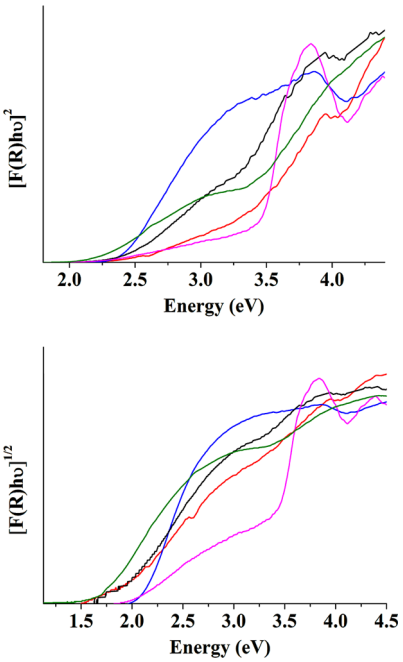

Figure 6. Tauc plots of $[F(R)h\nu]^n$ vs $[h\nu]$ for the direct and indirect bandgap sizes, $n = 2$ (upper) and $n = 1/2$ (lower), respectively, for **I** (pink line; terpy ligand), **II** (black line; bpym ligand), **III** (red line; *o*-phen ligand), **IV** (green line; 4,4′-bpy ligand), and $V_4O_{10}(o\text{-phen})_2$ (blue line).

highest-energy bandgap is found for **I**, ∼1.95 eV, containing the one-dimensional $[MnV_2O_6]_n$ chains and the terpyridine ligand. The hybrid structures containing extended $[MnV_2O_6]$ layers show lower-energy bandgap sizes within the range from ∼1.65 to ∼1.85 eV, that is, for **II** to **IV**. This results from the extended metal-oxide connectivity and higher band dispersion in these layered structures, as probed in the electronic structure calculations below. Hybrids **II** and **III** exhibit closely matching bandgap sizes of ∼1.85 to ∼1.90 eV as a result of their similarly connected $[MnV_2O_6]$ layers that are both constructed from chains of vertex-shared VO_4 tetrahedra linked together by the octahedral Mn(II) cations. In contrast, the structure of **IV** contains chains of edge-shared VO_5 square pyramids as well as chains of edge-shared octahedral Mn(II) cations, leading to the smallest bandgap size of this series at ∼1.65 eV. Thus, the dimensionality of the inorganic $[MnV_2O_6]$ network within each hybrid structure is found to be inversely related to the resulting bandgap size. The related hybrid $V_4O_{10}(o\text{-phen})_2$ exhibits a larger bandgap size of ∼2.1 eV, representing a blue shift of ∼0.15 to ∼0.45 eV compared to the Mn(II)-containing hybrids. This suggests that the addition of the Mn(II) $3d^5$ orbitals occurs at a slightly lower energy than the ligand π-based orbitals, with a moderate dependence on the structural dimensionality and the specific organic ligand, as described below.

C. Thermal Stability and Ligand Removal. The low-temperature removal of ligands from the structures of hybrid compounds may yield new routes to microporous and/or high surface area compounds. The thermal stabilities and decomposition products of **I** to **IV** and $V_4(o\text{-phen})_2O_{10}$ were investigated by heating in air or under flowing nitrogen with a ramping rate of 5 °C per minute. The thermogravimetric results of the weight losses versus temperature are shown in Figure 7 and Supporting Information, Figure S13. The post-

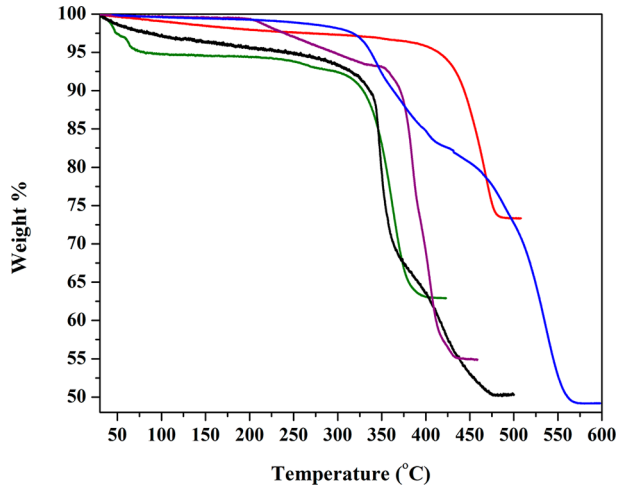

Figure 7. TGA of compounds $V_4O_{10}(o\text{-phen})_2$ (blue), **I** (black), **II** (red), **III** (purple), and **IV**(olive) under air with 5 °C/min ramping up, plotted as weight (%) vs temperature (°C).

TGA products were characterized by powder XRD and specific surface area BET analysis. In addition, the effect of the ligand removal on the bandgap size was probed by UV−vis DRS measurements. The experimental data are provided in the Supporting Information in Figures S8−S14, and a listing of the data is assembled in Table 4.

Hybrid compounds **I** to **IV** show a relatively similar range of thermal stabilities and exhibit the loss of structural water and organic ligands with heating. No significant differences are observed between samples heated in air or in nitrogen, and thus the results described below focus on the former. Shown in Figure 7, both **I** and **II** contain structural water that is lost gradually from ∼100 °C to ∼350−400 °C (**I**: expt. 2.98%, calcd. 3.57%; **II**: expt. 3.5%, calcd. 2.52%). However, in **III**, both the water and organic ligands are removed gradually starting at ∼200 to 450 °C (expt. 44.30%, calcd. 43.94%). While the structural water is coordinated to the Mn(II) cation in **III**, it is held more loosely in the structural cavities of **I** and **II** by hydrogen bonding. Larger structural pores containing water molecules are found in **IV** because of the longer bridging 4,4′-bpy ligands. As a result, in **IV** the water is observed to be removed in two sharper and well-defined steps at a much lower temperature of ∼50−75 °C (expt. 5.1%, calcd. 4.9%). Contrastingly, the structures of **I**, **II**, and **III**, that is, with either nonbridging ligands (*o*-phen or terpy) or a shorter

DOI: 10.1021/acs.inorgchem.5b00931
Inorg. Chem. 2015, 54, 7388−7401

bridging ligand (bpym), are gradually collapsing and causing the loss of the remaining structural water to become increasingly difficult and to extend over several hundreds of degrees. For **IV**, the sharp water loss at lower temperature is consistent with a noncollapsing structure.[22] The loss of the organic ligands eventually occurs at higher temperatures for all four hybrid compounds (**I**: expt. 43.15%, calcd. 46.27%; **II**: expt. ~22.71%, calcd ~23.21%; **III**: expt. 44.30%, calcd. 43.94%; **IV**: expt. 36.47%, calcd. 32.10%). Notably, **II** had the highest thermal stability, at up to ~500 °C, which can be attributed to the more compact network formed by the shortest bridging and chelating ligand bipyrimidine. By comparison, the hybrid $V_4O_{10}(o\text{-phen})_2$ shows two weight-loss steps starting at ~300 °C and ~413 °C, both corresponding to the removal of a single *o*-phen ligand (total loss: expt. 49.27%, calcd. 49.77%).

Characterization of the post-TGA products showed that hybrids **I** to **IV** had decomposed to yield the known MnV_2O_6 phase,[39] according to powder XRD. Thus, the full collapse and condensation of the inorganic network results in their common formation of a condensed manganese(II)−vanadate phase with a conservation of the Mn/V (1:2) molar ratio. The specific surface areas were also measured to investigate the impact of the different pathways of structural collapse. As shown in Table 4, the surface area of the MnV_2O_6 product is the lowest for **III** at ~7.1 m^2/g, in which both the structural water and organic ligand were removed together only at higher temperatures. For **I** and **II**, wherein the loss of structural water starts at lower temperatures and gradually continues a few hundred degrees, the surface area of MnV_2O_6 increases to a higher value of ~15−16 m^2/g. Lastly, the highest surface area is found for **IV** at ~41 m^2/g, which exhibits a distinct step for the low-temperature loss of water. Thus, the higher surface areas are directly related to the tendency of the hybrid compound to maintain its structure with the removal of water, which is prior to the higher-temperature removal of the organic ligands. By comparison, $V_4O_{10}(o\text{-phen})_2$ exhibits almost no change in specific surface area, measured at 3.6 m^2/g and 3.5 m^2/g before and after the thermally driven removal of the *o*-phen ligand.

The optical absorption spectra and bandgap sizes of the post-TGA products are listed in Table 4 and shown in Figure 8 and Supporting Information, Figure S14. The MnV_2O_6 products from **I** to **IV** exhibit similar bandgap sizes (indirect) in the range of 1.69−1.83 eV. The bandgap size of MnV_2O_6 from **IV** is notably blue-shifted by ~0.2−0.4 eV compared to the MnV_2O_6 products from **I** to **III**, likely owing to much smaller particle sizes in the quantum confinement regime. This result is also consistent with the high surface area of the MnV_2O_6 product of **IV**.

D. Photocatalytic Activities for Hydrogen Production.

The heterogeneous photocatalytic activities for water reduction of **I** to **IV** and $V_4O_{10}(o\text{-phen})_2$ were investigated as particle suspensions within a 20% aqueous methanol solution that were irradiated by visible light at an irradiant power density of ~1.0 W/cm^2. Each sample was surface-impregnated with a standard 1% (by weight) Pt surface cocatalyst, as described previously.[15,40,41] Powder XRD was used to confirm the stability of **I** to **IV** and $V_4O_{10}(o\text{-phen})_2$ under these photocatalysis testing conditions, as provided in the Supporting Information.

At room temperature, that is, 25 °C, the hybrid compounds were found to be photocatalytically inactive. However, measurable photocatalytic activities begin to emerge at reaction temperatures from ~5 °C to ~15 °C above room temperature. The lowest temperatures for measurable photocatalytic activities were observed at 30 °C for **III**, at 36 °C for **I**, and at 40 °C for **II**, **IV**, and $V_4O_{10}(o\text{-phen})_2$. Thus, photocatalytic activities were measured at both 30 and 40 °C for **III** and at 40 °C for **I**, **II**, **IV**, and $V_4O_{10}(o\text{-phen})_2$. Approximate turnover numbers for the amount of hydrogen produced per surface site were calculated based on the measured specific surface areas, and the average density of surface sites was calculated for various surface terminations of the crystal structures, as described previously.[15] Time course plots of the turnover numbers are shown in Figures 9 and 10. Compound **III**, with the lowest threshold temperature, exhibits a low photocatalytic

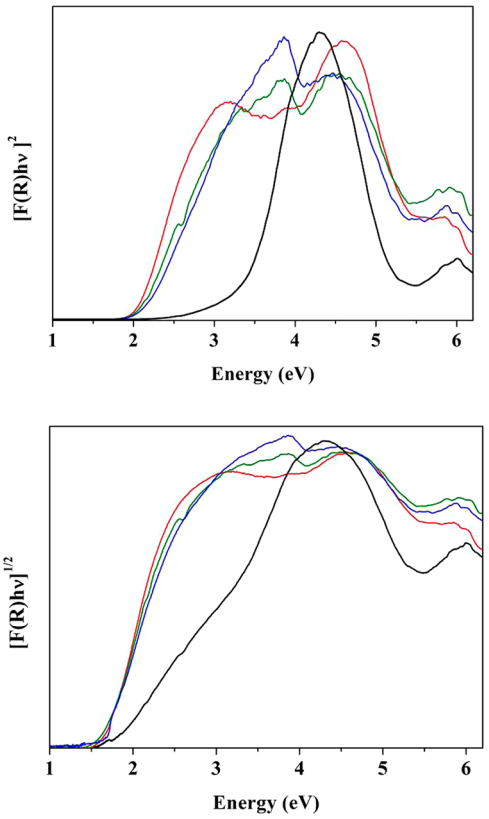

Figure 8. Tauc plots of $[F(R)h\nu]^n$ vs $[h\nu]$ for the direct and indirect bandgap sizes, $n = 2$ (upper) and $n = 1/2$ (lower), respectively, for the post-TGA MnV_2O_6 product in air obtained from **I** (green line; terpy ligand), **II** (blue line; bpym ligand), **III** (red line; *o*-phen ligand), and **IV** (black line; 4,4′-bpy ligand).

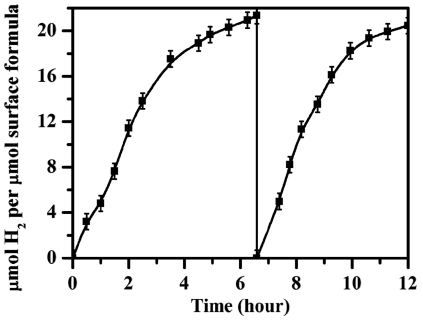

Figure 9. Photocatalytic hydrogen production rates per surface Pt sites of $Mn(H_2O)(o\text{-phen})V_2O_6$ (**III** ; ~10 mg) at 30 °C, with 1 wt % Pt as a surface cocatalyst suspended in a 20% methanol solution (~45 mL), under visible light (420−800 nm) at a radiant power density of 1 W/cm^2.

DOI: 10.1021/acs.inorgchem.5b00931
Inorg. Chem. 2015, 54, 7388−7401

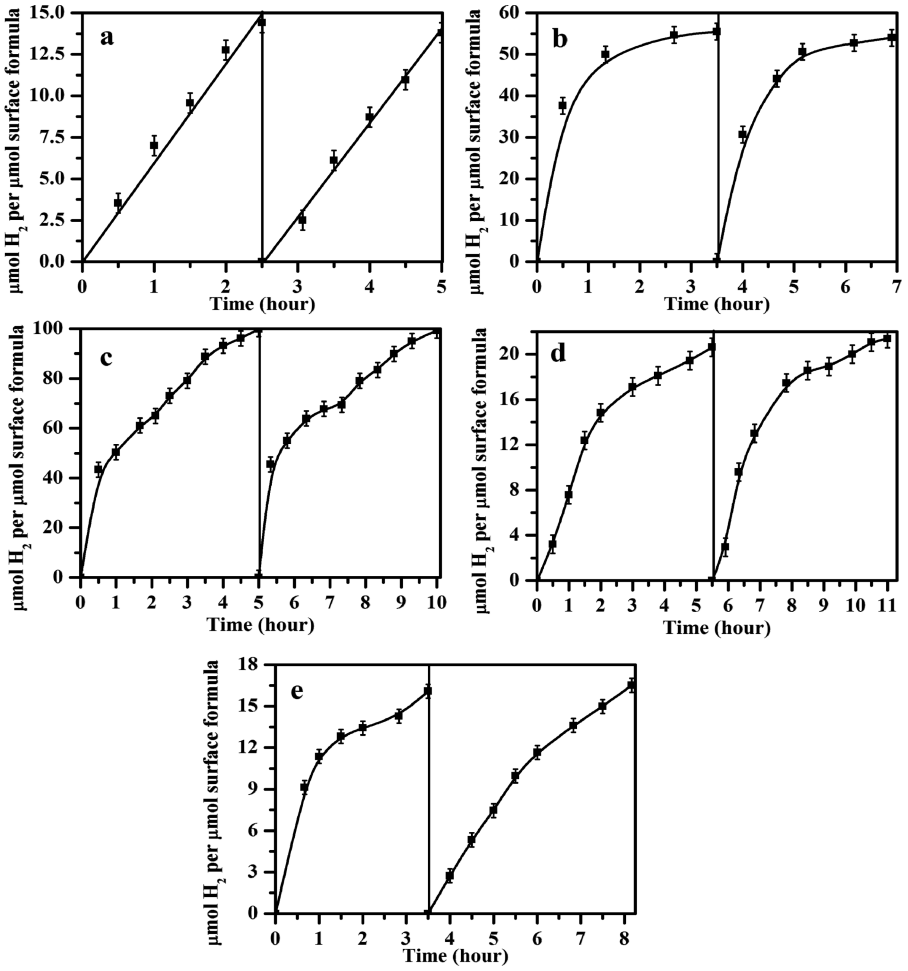

Figure 10. Photocatlaytic hydrogen production rates per surface Pt sites of (a) **I** ($Mn(terpy)V_2O_6{\cdot}H_2O$), (b) **II** ($Mn_2(bpym)V_4O_{12}{\cdot}0.6H_2O$), (c) **III** ($Mn(H_2O)(o\text{-phen})V_2O_6$), (d) **IV** ($Mn(4,4'\text{-bpy})V_2O_6{\cdot}1.16H_2O$), and (e) $V_4O_{10}(o\text{-phen})_2$. Testing conditions for hydrogen production included catalyst (~10 mg) with 1 wt % Pt as a surface cocatalyst suspended in a 20% methanol solution (~45 mL) under visible light (420−800 nm) at a radiant power density of 1 W/cm^2 at 40 °C.

rate of ~34 μmol H_2 $g^{-1}{\cdot}h^{-1}$ and a H_2 turnover frequency (TOF) of 4.6 h^{-1} at 30 °C, as shown in Figure 9. At 40 °C, the photocatalytic rate for **III** is tripled to ~91 μmol H_2 $g^{-1}{\cdot}h^{-1}$ and a TOF of 12.3 h^{-1}, as shown in Figure 10c. Similarly, for compound **I** at 40 °C, a constant production in the first 2.5 h of hydrogen at a rate of ~143 μmol H_2 $g^{-1}{\cdot}h^{-1}$, with a TOF of 5.7 h^{-1} at 40 °C is observed, as shown by vertical lines in Figure 10a. Compound **II** exhibits a high initial photocatalytic activity of ~673 μmol H_2 $g^{-1}{\cdot}h^{-1}$, with a TOF of 36.9 h^{-1} in the first 1.5 h at 40 °C, before gradually slowing to a stop after 4 h. However, its activity is fully recovered by washing and resuspending the catalyst powder in a fresh 20% methanol aqueous solution, as shown in Figure 10b. Similarly, compound **IV** exhibits a high initial photocatalytic rate of ~218 μmol H_2 $g^{-1}{\cdot}h^{-1}$ with a TOF of 7.2 h^{-1} in the first 3 h, before then stabilizing at a decreased rate of ~51 μmol H_2 $g^{-1}{\cdot}h^{-1}$ with a TOF of 1.7 h^{-1}; see Figure 10d. The related $V_4O_{10}(o\text{-phen})_2$ exhibited the lowest photocatalytic rates at 40 °C, at ~36 μmol H_2 $g^{-1}{\cdot}h^{-1}$ and a TOF of 3.6 h^{-1}, Figure 10e. For all compounds, the powdered catalysts could be dried and resuspended into a fresh aqueous methanol solution with a recovery of their photocatalytic activities, as shown in each of their time course plots in Figure 10.

Numerous prior studies have shown that the use of methanol as a hole scavenger most commonly results in its facile and complete oxidation to carbon dioxide. However, carbon dioxide was not detected by gas chromatography in any of these reactions. All post-reaction solutions exhibited a positive Tollen's test, with decreased pH values for **II** and **IV** (by ~0.5 to 1 units) and either unchanged or increased pH values for **I** and **III**. These results are consistent with the partial oxidation of methanol to formic acid for photocatalytic reactions involving **II** and **IV**, and to formaldehyde for **I** and **III**. Similarly, photocatalytic reactions involving Cu(I)- and Cu(II)-molybdate hybrids were also recently shown to result in the formation of formic acid and formaldehyde, rather than the complete oxidation of methanol to carbon dioxide.[42] Further, the photocatalytic rates of these hybrid compounds decrease most significantly with time for **II** and **IV**, which requires heating to the higher temperature of 40 °C. The increased photocatalytic rates at higher temperatures results from the faster adsorption/desorption rates at the surfaces of metal oxides. Thus, the higher required temperature and the slowing photocatalytic rates with time is most likely associated with the coordination of formic acid at the Mn(II) sites at the surfaces, which are shown to be the sites of photogenerated hole formation for oxidation (see Electronic Structure Calculations, described below). The detachment of the formate anion from the Mn(II) sites must represent a key barrier to completing the photocatalytic cycle. By comparison, the photocatalytic

DOI: 10.1021/acs.inorgchem.5b00931
Inorg. Chem. 2015, 54, 7388−7401

reactions involving **I** and **III** require lower temperatures and exhibit moderately less slowing of their rates with time.

E. Characterization and Effect of Metallic Surface Cocatalysts. The photodeposition of surface metal cocatalysts (e.g., Pt, Ni, or Cu) was investigated by SEM to probe the origin of the photocatalytic hydrogen production rates. Hybrids **I** and **III** were selected according to their photocatalytic activities that either rapidly degraded (e.g., <5 h for **I**) or remained nearly continuous for several hours (e.g., >6 h for **III**), as shown in Figure 10. The sizes and morphologies of the surface Pt cocatalysts, loaded at ∼10 wt % on **I** and **III**, are observed in the SEM images in Figures 11 and 12. The

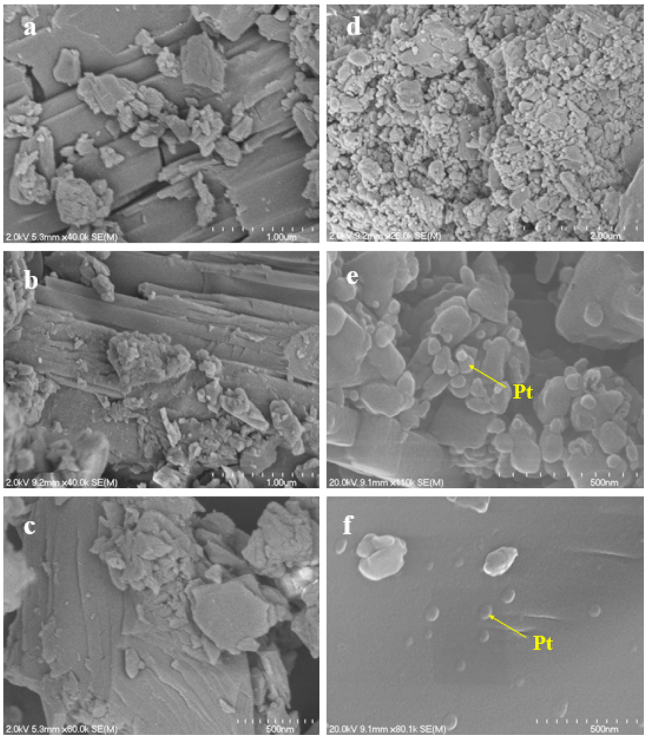

Figure 11. SEM images of **III** before (a–c) and after (d–f) photodeposition of 10 wt % platinum on the particle surfaces. The spherical surface islands, labeled with yellow arrows, are Pt particles.

crystallite surfaces are generally flat and smooth with typical dimensions spanning several micrometers. After photodeposition, surface islands of Pt are found that range in diameter from ∼25 to 60 nm, as confirmed by energy-dispersive X-ray spectroscopy measurements given in the Supporting Information (Figure S23). For hybrid **III**, the surface Pt islands tend to be semispherical and anchored well to the particle surfaces, Figure 11f. For hybrid **I**, by contrast, the surface Pt islands are more fully spherical and relatively not as well-attached to the particle surfaces, Figure 12d,e. This may account for the more rapid decay of the photocatalytic activity of **I**, as the Pt particles detach from the surfaces during the course of the reaction.

Alternate metal cocatalysts, that is, Ni and Cu, were photodeposited to probe the impact of the type of metal surface sites. As shown in Figure 13, the visible-light photocatalytic activities of **III** (at 40 °C) with 5 wt % Cu, Ni, or Pt were compared under identical photocatalytic reaction conditions. The use of 5 wt % Pt results in a higher photocatalytic rate of ∼106 μmol H_2 $g^{-1}{\cdot}h^{-1}$ and a H_2 TOF of 14.3 h^{-1}, as compared to the slightly lower activity with 1 wt

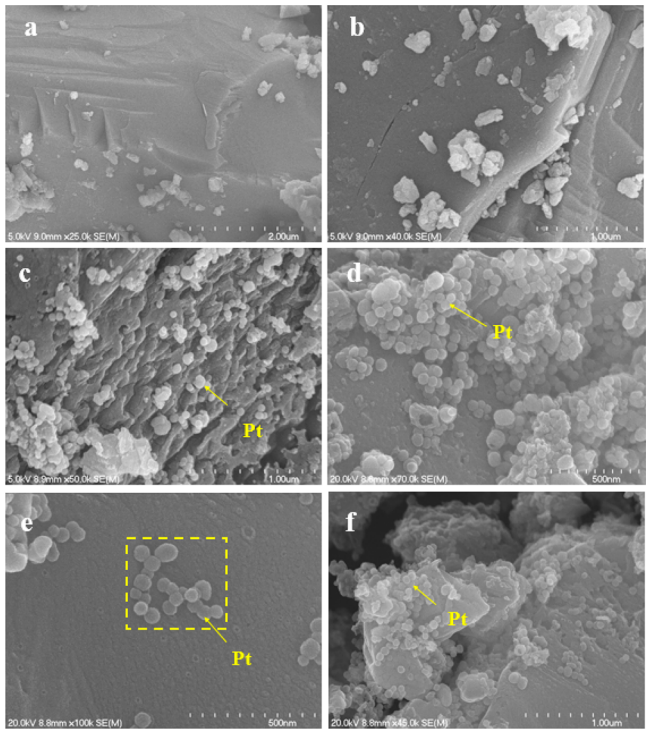

Figure 12. SEM images of **I** before (a, b) and after (c–f) photodeposition of 10 wt % platinum on the particle surfaces. The spherical surface islands, labeled within the yellow box and arrows, are Pt particles.

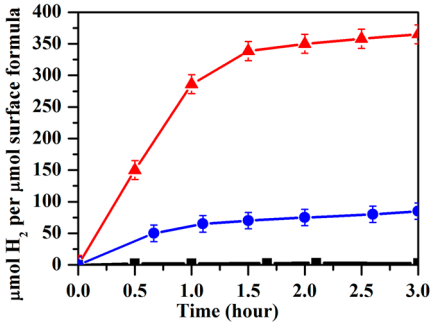

Figure 13. Photocatalytic hydrogen production rates per surface formula unit of **III**. The different surface cocatalysts (∼10 mg) were 5 wt % Ni (red), 5 wt % Pt (blue), and 5 wt % Cu (black); the material was suspended in a 20% methanol solution (∼45 mL) and irradiated under visible light (420–800 nm) at a power density of 1 W/cm^2 at 40 °C.

% Pt described above. However, no photocatalytic activity was detectable with 5 wt % Cu. Contrastingly, the photodeposition of 5 wt % Ni yields a significantly higher photocatalytic rate of ∼257 μmol H_2 $g^{-1}{\cdot}h^{-1}$ and a H_2 TOF of 34.8 h^{-1}. The photocatalytic activity with 5 wt % Ni is ∼2.4 times higher than that for 5 wt % Pt. Owing to the smaller atomic weight of Ni versus Pt (by a factor of ∼3.3), a greater amount of Ni is deposited onto the particle surfaces, which accounts for much of the increase. The metal cocatalysts aid in the charge separation of the electron/hole pairs at the surfaces. Thus, a larger amount of surface cocatalysts can facilitate a higher photocatalytic rate, especially for materials with a limited mobility of the photoexcited charge carriers. Further research is

DOI: 10.1021/acs.inorgchem.5b00931
Inorg. Chem. 2015, 54, 7388–7401

necessary to more deeply elucidate the roles of the surface metal cocatalyts.

F. Electronic Structure Calculations. Electronic structure calculations of compounds **I**, **II**, and **III** were performed using density-functional theory methods to probe the structural origins of their optical bandgap sizes and photocatalytic reactions. Plots of the electron density at the conduction and valence band edges are shown for each in Figures 14−16

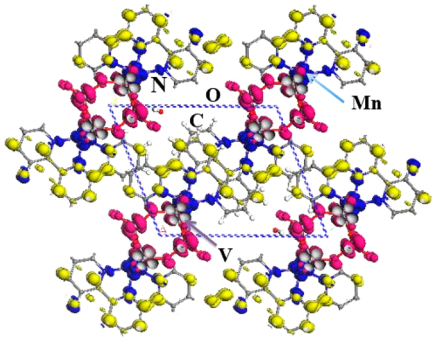

Figure 14. Plot of the electron densities of the HOCO (blue), LUCO (pink), and the second LUCO (yellow) of **I** (Mn(terpy)V_2O_6·H_2O).

(overlaid onto their structures), and the total and partial densities-of-states are given in Figures S5−S7 in the Supporting Information. The highest-occupied crystal orbitals (HOCO) for all three hybrids primarily consist of the half-filled d^5 orbital contributions from Mn, with some contributions from the N 2p orbitals from the respective organic ligands. For **I** and **II**, Figures 14 and 15, the lowest-unoccupied crystal orbitals

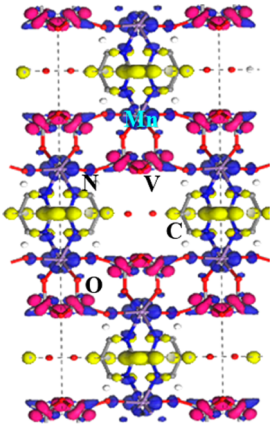

Figure 15. Plot of the electron densities of the HOCO (blue), LUCO (pink), and second LUCO (yellow) of **II** (Mn_2(bpym)V_4O_{12}·$0.6H_2O$).

(LUCOs) consist of empty V 3d orbital contributions, with a bandgap transition corresponding to a charge transfer between the Mn- and V-based valence and conduction band states, respectively. The ligand 2p orbital contributions, that is, empty π^* orbitals found at slightly higher energies within the conduction bands of both, must also contribute significantly to bandgap light absorption. In comparison, the LUCOs of **III**, shown in Figure 16, are found to consist of π^* orbital contributions from the *o*-phen ligands, with the V 3d orbital contributions at slightly higher energies. This is attributed to the π^* orbitals in bpym and terpyridine being located at relatively higher energies than those in *o*-phen. Among these

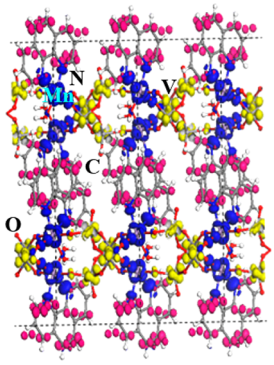

Figure 16. Plot of the electron densities of the HOCO (blue), LUCO (pink), and second LUCO (yellow) of **III** (Mn(H_2O)(*o*-phen)V_2O_6).

three hybrids, **III** has the lowest threshold temperature for visible-light photocatalytic activity, which could be related to the different energetic ordering of the V 3d and ligand π^* orbitals at the bottom of the conduction bands.

As described above, the π^* ligand and V 3d orbitals are found to be located at similar energies within these hybrid compounds. While these differences are relatively minor and difficult to differentiate by these methods, both metal-to-ligand and metal-to-metal excitations must be contributing to bandgap absorption. Thus, the removal of the organic ligands in **I** to **IV**, yielding MnV_2O_6, results in a closely similar bandgap size to the hybrids (described above). Electron density plots for V_4O_{10}(*o*-phen)$_2$ are shown in Figure 17 for comparison to the Mn(II)-

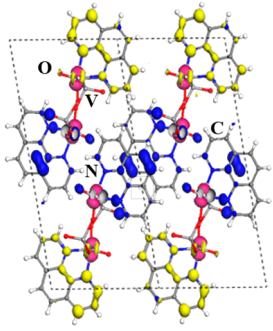

Figure 17. Plot of the electron densities of the HOCO (blue), LUCO (pink), and second LUCO for V_4O_{10}(*o*-phen)$_2$.

containing hybrids. In this case the HOCO consist of the N 2p σ-orbitals from the ligand rather than the manganese d^5 orbitals. This is consistent with the removal of manganese leading to an increase in the bandgap size, that is, found by comparing the relatively larger bandgap size of V_4O_{10}(*o*-phen)$_2$ versus that in the related Mn(H_2O)(*o*-phen)V_2O_6 (**III**) in Table 4. Conversely, the bottom of the conduction band of V_4O_{10}(*o*-phen)$_2$ consists of the empty V d-orbitals in Figure 15, with the empty π^* orbitals on the *o*-phen at slightly higher energies. The coordinating organic ligands thus modify the dimensionality of the inorganic [MnV_2O_6] components within each hybrid compound, resulting in significant modifications of their bandgap sizes and photocatalytic activities. The [MnV_2O_6]$_n$ chains in **I** result in the largest bandgap size, and its densities-of-states are shown to exhibit the least amount of band dispersion in Supporting Information, Figure S5. By comparison, larger band dispersions are calculated for **II** and **III**

DOI: 10.1021/acs.inorgchem.5b00931
Inorg. Chem. 2015, 54, 7388−7401

that contain extended $[MnV_2O_6]$ layers, consistent with the smaller bandgap sizes.

IV. CONCLUSIONS

The family of four manganese(II)−vanadate(V)/organic hybrids, namely, $Mn(terpy)V_2O_6{\cdot}H_2O$ (**I**), $Mn_2(bpym)V_4O_{12}{\cdot}0.6H_2O$(**II**), $Mn(o\text{-phen})V_2O_6{\cdot}H_2O$ (**III**), and $Mn(4,4'\text{-bpy})V_2O_6{\cdot}1.16H_2O$(**IV**), was investigated for the impacts of the organic ligands upon local coordination geometries and the extended $[MnV_2O_6]$ network dimensionality. The organic ligands coordinate preferentially to the Mn(II) sites, and the coordination geometries and numbers have the predominant effect on whether $[MnV_2O_6]$ chains (in **I**) or $[MnV_2O_6]_n$ layers (in **II**, **III**, and **IV**) are formed. The optical bandgap sizes fall in the range from ∼1.65 to ∼1.95 eV and increase with decreasing network dimensionality. When the hybrid is heated in air or nitrogen, the loss of structural water occurs gradually for **I**, **II**, and **III** over several hundreds of degrees, while the structural water is lost at closer to room temperature for **IV**. At higher temperatures the condensed MnV_2O_6 phase forms after the loss of both structural water and organic ligands from each hybrid. The specific surface areas of the MnV_2O_6 products range from ∼7 m^2/g for **III** to ∼41 m^2/g for **IV**. The longer bridging 4,4′-bipyridine in **IV** helps to inhibit the collapse of the inorganic network, thus leading to the highest surface area of the MnV_2O_6 product. The blue-shifted bandgap size of MnV_2O_6 obtained from **IV** indicates particle sizes in the quantum confinement regime, as compared to **I**, **II**, and **III** with consistent bandgap sizes of ∼1.7 eV. Compounds **I** to **IV** exhibit temperature-dependent visible-light photocatalytic activities for hydrogen production in 20% methanol solutions, with their activities increasing with the oxide/organic network connectivity. In contrast, the related $V_4O_{10}(o\text{-phen})_2$ exhibits a larger bandgap size and significantly lower hydrogen production rate. Electronic structure calculations show that the band edges are primarily derived from the half-filled Mn $3d^5$ in the valence band and the empty V $3d^0$ and ligand π^* orbital contributions in the conduction band. These results demonstrate that coordinating organic ligands can serve a prominent role in directing the inorganic components within hybrid structures and modulating their chemical and physical properties.

■ ASSOCIATED CONTENT

Supporting Information

Relevant powder XRD patterns, infrared spectra, UV−vis spectra, thermogravmetric data, EPR spectra, SEM images, and the calculated total and partial densities-of-states for the hybrid structures are available. The Supporting Information is available free of charge on the ACS Publications website at DOI: 10.1021/acs.inorgchem.5b00931.

■ AUTHOR INFORMATION

Corresponding Author

*E-mail: Paul_Maggard@ncsu.edu.

Notes

The authors declare no competing financial interest.

■ ACKNOWLEDGMENTS

Support is acknowledged from Dr. R. Sommer for assistance with the collection of single-crystal X-ray data. The authors also thank the Research Corporation for Science Advancement (P.M. is a Scialog Awardee) and the Dept. of Chemistry at North Carolina State Univ. for financial support of this research.

■ DEDICATION

Dedicated to Professor John D. Corbett.

■ REFERENCES

(1) Vallet-Regi, M.; Colilla, M.; Gonzalez, B. *Chem. Soc. Rev.* **2011**, *40*, 596−607.
(2) Ma, S.; Zhou, H.-C. *Chem. Commun.* **2010**, *46*, 44−53.
(3) Gómez-Romero, P.; Chojak, M.; Cuentas-Gallegos, K.; Asensio, J. A.; Kulesza, P. J.; Casañ-Pastor, N.; Lira-Cantú, M. *Electrochem. Commun.* **2003**, *5*, 149−153.
(4) Kataoka, Y.; Sato, K.; Miyazaki, Y.; Masuda, K.; Tanaka, H.; Naito, S.; Mori, W. *Energy Environ. Sci.* **2009**, *2*, 397−400.
(5) Fateeva, A.; Chater, P. A.; Ireland, C. P.; Tahir, A. A.; Khimyak, Y. Z.; Wiper, P. V.; Darwent, J. R.; Rosseinsky, M. J. *Angew. Chem., Int. Ed.* **2012**, *51*, 7440−7444.
(6) (a) Hagrman, P. J.; Hagrman, D.; Zubieta, J. *Angew. Chem., Int. Ed.* **1999**, *38*, 2638−2684. (b) Armatas, N. G.; Ouellette, W.; Whitenack, K.; Pelcher, J.; Liu, H.; Romaine, E.; O'Connor, C. J.; Zubieta, J. *Inorg. Chem.* **2009**, *48*, 8897−8910. (c) Jones, S.; Vargas, J. M.; Pellizzeri, S.; O'Connor, C. J.; Zubieta, J. *Inorg. Chim. Acta* **2013**, *395*, 44−57.
(7) Lin, H.; Wu, X.; Maggard, P. A. *Inorg. Chem.* **2009**, *48*, 11265−11276.
(8) Kim, J.; Chen, B.; Reineke, T. M.; Li, H.; Eddaoudi, M.; Moler, D. B.; O'Keeffe, M.; Yaghi, O. M. *J. Am. Chem. Soc.* **2001**, *123*, 8239−8247.
(9) Oshikiri, M.; Boero, M.; Ye, J.; Zou, Z.; Kido, G. *J. Chem. Phys.* **2002**, *117*, 7313−7318.
(10) Shen, T. F. R.; Lai, M.-H.; Yang, T. C. K.; Fu, I. P.; Liang, N.-Y.; Chen, W.-T. *J. Taiwan Inst. Chem. Eng.* **2012**, *43*, 95−101.
(11) Konta, R.; Kato, H.; Kobayashi, H.; Kudo, A. *Phys. Chem. Chem. Phys.* **2003**, *5*, 3061−3065.
(12) (a) Hagrman, P. J.; Finn, R. C.; Zubieta, J. *Solid State Sci.* **2001**, *3*, 745−774. (b) de Luis, R. F.; Orive, J.; Larrea, E. S.; Urtiaga, M. K.; Arriortua, M. I. *CrystEngComm* **2014**, *16*, 10332−10366.
(13) Lin, H.; Maggard, P. A. *Inorg. Chem.* **2008**, *47* (18), 8044−8052.
(14) Li, S.; Sun, W.; Wang, K.; Ma, H.; Pang, H.; Liu, H.; Zhang, J. *Inorg. Chem.* **2014**, *53*, 4541−4547.
(15) Luo, L.; Maggard, P. A. *Cryst. Growth Des.* **2013**, *13*, 5282−5288.
(16) (a) Smith, T. M.; Freund, S. R.; Lau, A.; Varges, J.; Spinu, L.; Zubieta, J. *Inorg. Chim. Acta* **2014**, *414*, 91−96. (b) Hu, Y.; Luo, F.; Dong, F. *Chem. Commun.* **2011**, *47*, 761−763.
(17) Wu, Q.; Hao, W.; Feng, X.; Wang, Y.; Li, Y.; Wang, E.; Zhu, X.; Pan, X. *Inorg. Chem. Commun.* **2012**, *22*, 137−140.
(18) Abbood, H.; Ahmed, K.; Ren, Y.; Huang, K. *Appl. Phys. A: Mater. Sci. Process.* **2013**, *112*, 901−909.
(19) Nandini Devi, R.; Zubieta, J. *Inorg. Chim. Acta* **2002**, *338*, 165−168.
(20) Li, Y.; Wang, E.; Zhang, H.; Luan, G.; Hu, C.; Hu, N.; Jia, H. *J. Solid State Chem.* **2002**, *163*, 10−16.
(21) McCann, S.; McCann, M.; Casey, M. T.; Jackman, M.; Devereux, M.; McKee, V. *Inorg. Chim. Acta* **1998**, *279*, 24−29.
(22) Fernández de Luis, R.; Urtiaga, M.; Mesa, J.; Vidal, K.; Lezama, L.; Rojo, T.; Arriortua, M. *Chem. Mater.* **2010**, *22*, 5543−5553.
(23) Bruker-Nonius. *SAINT;* Bruker AXS Inc.: Madison, WI, 2007.
(24) Sheldrick, G. *Acta Crystallogr., Sect. A: Found. Crystallogr.* **2008**, *64*, 112−122.
(25) *Reflectance Spectroscopy;* Kortüm, G., Ed.; Springer-Verlag: Berlin, Germany, 1969.
(26) Yu, J.; Kudo, A. *Adv. Funct. Mater.* **2006**, *16*, 2163−2169.
(27) Alaouie, A. M.; Smirnov, A. I. *J. Magn. Reson.* **2006**, *182*, 229−238.

DOI: 10.1021/acs.inorgchem.5b00931
Inorg. Chem. 2015, 54, 7388−7401

(28) Clark, S. J.; Segall, M. D.; Pickard, C. J.; Hasnip, P. J.; Probert, M. I. J.; Refson, K.; Payne, M. C. *Zeitsch. Kristall. Crystall. Mater.* **2005**, *220*, 567.
(29) Payne, M. C.; Teter, M. P.; Allan, D. C.; Arias, T. A.; Joannopoulos, J. D. *Rev. Mod. Phys.* **1992**, *64*, 1045−1097.
(30) Monkhorst, H. J.; Pack, J. D. *Phys. Rev.* **1976**, *13*, 5188−5192.
(31) Naito, R.; Ohta, K.; Shirai, H. *J. Porphyrins Phthalocyanines* **2001**, *5*, 44−50.
(32) Postmus, C.; Ferraro, J. R.; Woznizk, W. *Inorg. Chem.* **1967**, *6*, 2030−2032.
(33) Leroux, F.; Piffard, Y.; Ouvrard, G.; Mansot, J. L.; Guyomard, D. *Chem. Mater.* **1999**, *11*, 2948−2959.
(34) Nandini Devi, R.; Zubieta, J. *Inorg. Chim. Acta* **2003**, *343*, 313−316.
(35) Jaradat, Q.; Barqawi, K.; Akasheh, T. S. *Inorg. Chim. Acta* **1986**, *116*, 63−73.
(36) Bagshaw, S. A.; Cooney, R. P. *Appl. Spectrosc.* **1996**, *50*, 310−315.
(37) Tronconi, A. L.; Morais, P. C.; Pelegrini, F.; Tourinho, F. A. *J. Magn. Magn. Mater.* **1993**, *122*, 90−92.
(38) Drzewiecki, A.; Padlyak, B.; Adamiv, V.; Burak, Y.; Teslyuk, I. *Nukleonika* **2013**, *58*, 379−385.
(39) Kim, S.-S.; Ikuta, H.; Wakihara, M. *Solid State Ionics* **2001**, *139*, 57−65.
(40) Arney, D.; Hardy, C.; Greve, B.; Maggard, P. A. *J. Photochem. Photobiol., A* **2010**, *214*, 54−60.
(41) Arney, D.; Watkins, T.; Maggard, P. A. *J. Am. Ceram. Soc.* **2011**, *94* (5), 1483−1489.
(42) Luo, L.; Lin, H.; Li, L.; Smirnova, T. I.; Maggard, P. A. *Inorg. Chem.* **2014**, *53*, 3464−3470.

DOI: 10.1021/acs.inorgchem.5b00931
Inorg. Chem. 2015, 54, 7388−7401